PHYSICAL REVIEW MATERIALS **8**, 063603 (2024)

Androgynous $\{10\bar{1}2\}$ twin in zinc

Sébastien Merkel[*] and Nadège Hilairet
Univ. Lille, CNRS, INRAE, Centrale Lille, UMR 8207 - UMET - Unité Matériaux et Transformations, F-59000 Lille, France

Yanbin Wang
Center for Advanced Radiation Sources, University of Chicago, Chicago, Illinois 60637, USA

Jérémy Guignard[†]
ESRF European Synchrotron, F-38000 Grenoble, France

Carlos N. Tomé
Materials Science and Technology Division, Los Alamos National Laboratory, Los Alamos, New Mexico 87545, USA

(Received 3 April 2024; accepted 21 May 2024; published 10 June 2024)

Under ambient conditions, Zn is a hexagonal metal with a large c/a ratio of 1.856. Plastic deformation is predominantly accommodated by basal $\langle a\rangle$ slip and compression twins on the $\{10\bar{1}2\}$ planes. Increasing hydrostatic pressure drastically reduces the c/a ratio of Zn and, when a critical threshold of $c/a = \sqrt{3}$ at about 10 GPa is crossed, the $\{10\bar{1}2\}$ twins are predicted to change from compressive to tensile in nature. What happens at the transition point, when $c/a = \sqrt{3}$, remains unknown. Here, we strain-cycle a textured polycrystalline sample of pure Zn at uniform hydrostatic pressures ranging between 2 and 17 GPa, over which the c/a ratio crosses the $c/a = \sqrt{3}$ compressive-tensile transition for $\{10\bar{1}2\}$ twins. During deformation, the state of the sample is monitored *in situ* through x-ray diffraction to extract texture and internal strain evolution. By comparing the experimental results with the predictions of an elastoviscoplastic polycrystal simulation, we confirm the androgynous nature of $\{10\bar{1}2\}$ twin response at low and high pressures. When $c/a = \sqrt{3}$, polycrystalline Zn does not display any evidence of twinning and its plastic behavior is controlled by mostly basal and pyramidal $\langle c + a\rangle$ slip activity, with a very small contribution of prismatic $\langle a\rangle$ slip. Evidence for the activity of other $\{10\bar{1}n\}$ twinning modes, which have been suggested for Zn under high pressure, are not observed.

DOI: 10.1103/PhysRevMaterials.8.063603

I. INTRODUCTION

Hexagonal-closed-packed (hcp) metals, such as titanium, zirconium, magnesium, zinc, cobalt, etc., are extensively used in a variety of industrial applications [1–3]. They are also of interest in the earth and planetary sciences because the interior structure of the Earth and other planets is formed by hcp Fe under (exo)planetary core pressure [4]. In contrast to more common metals with a cubic structure, however, hcp metals exhibit distinct mechanical behavior, with fewer available slip systems and significant contribution of deformation twinning [5]. The latter often dominates the formation of crystallographic textures. Twinning, in fact, enables deformation of the lattice that would otherwise be difficult to accommodate, but the resulting twin-reoriented microstructures and anisotropy of mechanical properties can impede the potential applications of hcp metals [6]. As such, twinning in hcp metals is an active field of research, both under ambient and extreme conditions [7–10].

Shears and reorientations associated with twinning in hcp metals depend on the material's c/a ratio (Fig. 1). Twins can be either tensile or compressive, depending on whether the associated shear leads to a lengthening or a shortening along the crystal's c axis. In this regard, $\{10\bar{1}2\}$ twinning is peculiar in that its tensile or compressive nature depends on the value of the c/a ratio. For metals with $c/a > \sqrt{3} \approx 1.723$, $\{10\bar{1}2\}$ twins are compressive, while for those with $c/a < \sqrt{3}$, $\{10\bar{1}2\}$ twins are tensile (Fig. 1).

Cd and Zn differ from all other hcp metals in that their c/a ratio greatly exceeds the ideal $\sqrt{8/3} \approx 1.633$ value, and also exceeds the threshold value of $\sqrt{3}$ which marks the transition from tensile to compressive $\{10\bar{1}2\}$ twins (Fig. 1). Even more interesting, both Zn and Cd c/a ratios can be tuned by applied hydrostatic pressure [11]. In the case of Zn, for instance, $c/a = 1.856$ under ambient pressure, it decreases to $\sqrt{3}$ at about 10 GPa and crosses the ideal value of $\sqrt{8/3}$ at about 50 GPa [12–15]. Zn and Cd are hence ideal candidates to test how crystallographic models handle the effect of varying c/a ratios on hcp metal plasticity.

---

[*] sebastien.merkel@univ-lille.fr

[†] Present address: IROX Technology, Toulouse, France.

Published by the American Physical Society under the terms of the Creative Commons Attribution 4.0 International license. Further distribution of this work must maintain attribution to the author(s) and the published article's title, journal citation, and DOI.

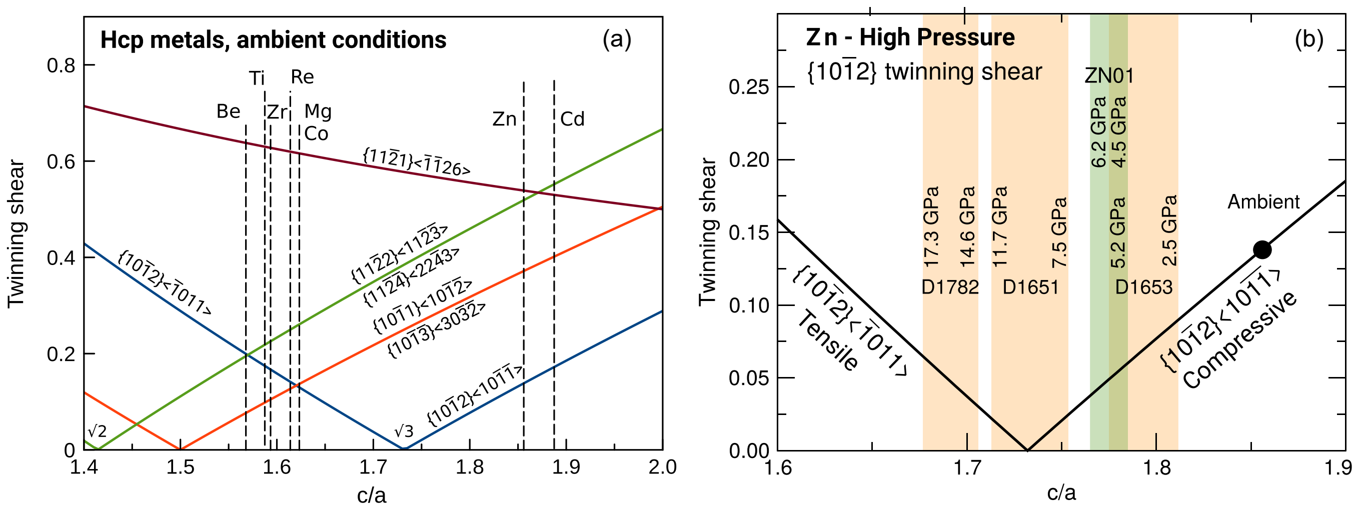

FIG. 1. (a) Variation of twinning shear with c/a ratio in hcp crystals along with ambient condition values of c/a for eight common hcp metals; see Ref. [5]. $\{11\bar{2}1\}$ twinning is always tensile, while the other twinning modes can be either tensile or compressive, depending on the c/a ratio. (b) $\{10\bar{1}2\}$ twinning shear as a function of c/a ratio for Zn with increasing pressure. Experiments Zn01 and D1653 are performed in the 2.5–6.2 GPa pressure range at which $c/a > \sqrt{3}$ and for which $\{10\bar{1}2\}$ twins should be compressive. Experiment D1782 is performed in the 14.6–17.3 GPa pressure range at which $c/a < \sqrt{3}$ and for which $\{10\bar{1}2\}$ should be tensile. Finally, experiment D1651 is performed at pressures in the 7.5–11.7 GPa pressure range at which $c/a \approx \sqrt{3}$. In such cases, $\{10\bar{1}2\}$ twins cannot contribute to plastic strain and should be replaced by an alternative deformation mechanism.

Plasticity of Zn at room temperature and pressure takes place mainly by activation of basal slip and $\{10\bar{1}2\}$ compressive twins [3]. According to Ref. [5], the characteristic shear of the $\{10\bar{1}2\}$ twin system is

$$S = \left|\frac{(c/a)^2 - 3}{(c/a)\sqrt{3}}\right|, \tag{1}$$

with a Burgers vector $\bar{\mathbf{b}} = \eta_1\langle 10\bar{1}\bar{1}\rangle$ if $c/a > \sqrt{3}$, and a Burgers vector $\bar{\mathbf{b}} = \eta_1\langle\bar{1}011\rangle$ if $c/a < \sqrt{3}$ (here, $\eta_1 = |\frac{(c/a)^2-3}{(c/a)^2+3}|$). The volume fraction of the crystal, f^{tw}, required to accommodate a twin shear $\Delta\gamma^{\mathrm{tw}}$ is

$$f^{\mathrm{tw}} = \frac{\Delta\gamma^{\mathrm{tw}}}{S}. \tag{2}$$

When $c/a < \sqrt{3}$, the Burgers vector reverses to $\langle\bar{1}011\rangle$ and the twin should become tensile. It is apparent from Eq. (1), however, that when c/a is close to $\sqrt{3}$ (which happens at about 10 GPa), the characteristic shear S is very small and, according to Eq. (2), even accommodating a small amount of shear via $\{10\bar{1}2\}$ twins would involve the reorientation of the entire crystal.

The large pressure dependence of Zn's c/a ratio hence raises a number of intriguing questions:

(i) Does twin reorientation still take place in the vicinity of $c/a = \sqrt{3}$, despite $\{10\bar{1}2\}$ twinning affecting the whole grain without contributing to strain?

(ii) What are the active deformation systems in Zn in the vicinity of $c/a = \sqrt{3}$, in case twinning should not contribute shear?

(iii) Are $\{10\bar{1}2\}$ tensile twins active when $c/a < \sqrt{3}$, as Fig. 1 would suggest, or is deformation purely accommodated by slip? And, if so, which are the active slip systems?

(iv) Can twins be reversed through detwinning processes?

Kanitpanyacharoen *et al.* [16] studied the effect of hydrostatic pressure on texture evolution in polycrystalline Cd, Os, Zn, and Hf based on experiments in the diamond anvil cell and the multi-anvil deformation device known as the deformation DIA (D-DIA). In their experiment, compression texture in Zn was shown to strengthen past 10 GPa, which the authors associated to a change in nature of $\{10\bar{1}2\}$ twins, switching from compressive to tensile in nature due to the change in c/a ratio. In another study, density functional theory calculations were used to evaluate the effect of pressure on the c/a ratio and twin boundary formation energy for $\{10\bar{1}1\}$, $\{10\bar{1}2\}$, and $\{10\bar{1}3\}$ twins in Zn [17]. The calculations showed that the formation energy increases with pressure for all of them, being comparable for $\{10\bar{1}2\}$ and $\{10\bar{1}3\}$, and lower than the one for $\{10\bar{1}1\}$. However, at pressures higher than 25 GPa, well into the range where $c/a < \sqrt{3}$, the energy of the $\{10\bar{1}2\}$ twin boundary shows a sudden increase. The authors hence concluded that pressure could change the active twinning modes of Zn past such threshold. Overall, the activity of $\{10\bar{1}2\}$ twins in Zn near $c/a = \sqrt{3}$ and at higher pressures deserves further investigation.

The purpose of this work is hence to focus on the effect of hydrostatic pressure on the plastic behavior of Zn, to understand the respective roles of twinning and slip systems with changes in c/a ratio, and the associated material's strength and microstructures. Millimetric samples of pure Zn are subjected to cycles of tension and compression under pressures chosen to reveal the compressive, transitional, and tensile character of $\{10\bar{1}2\}$ twins (Fig. 1). Texture and internal strain evolution are measured *in situ* using synchrotron x-ray diffraction, and elastoviscoplastic self-consistent (EVPSC) modeling is performed to identify the possible slip and twin system activity leading to the observed textures and internal strains. Of particular interest is the characterization of the reversibility of the twin domains. We then use our experimental results to

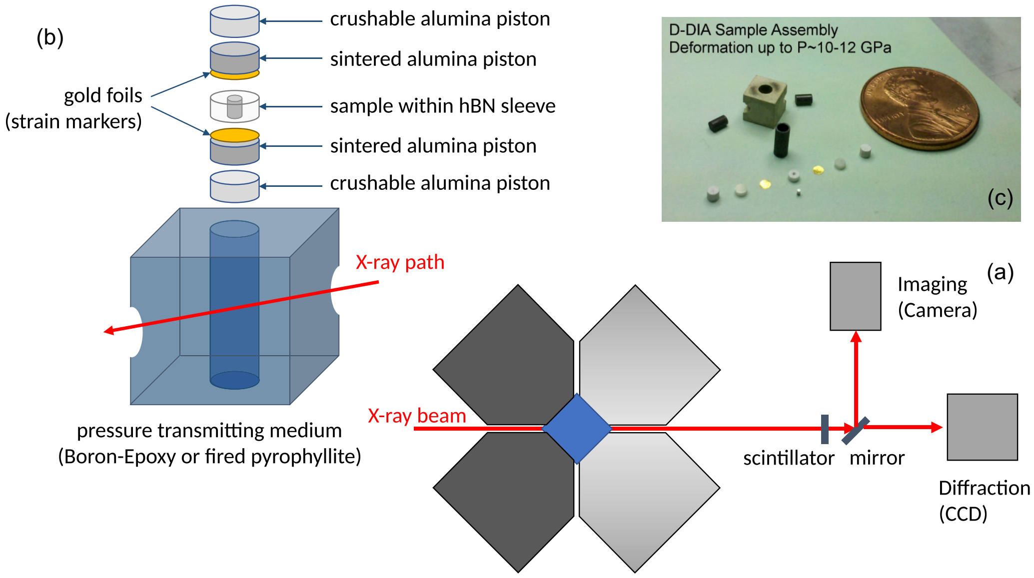

FIG. 2. Experimental setup for deformation experiments in the D-DIA. (a) The sample assembly (blue) is confined between four lateral and two vertical (not shown) anvils. Hydrostatic pressure is obtained by advancing all six anvils simultaneously. Axial compression (sample shortening) is obtained by advancing the two vertical anvils and retracting the four lateral anvils. Lateral compression (sample lengthening) is reached by advancing the four lateral anvils and retracting the two vertical anvils. The incoming x-ray beam passes through the entire assembly. Two sintered-diamond anvils (light gray) are used downstream to allow collection of alternating radiographic and diffraction images to characterize the sample. (b) Schematic of the high-pressure cell assembly, with slight variations depending on the pressure investigated, and (c) picture of the cell for the 10–12 GPa experiment, in which the pressure medium was a fired pyrophyllite cube with boron epoxy x-ray transparent windows. The black sleeve is graphite furnace, which is part of the assembly but not used during the experiment. The small shiny rod in the front is a 0.5-mm-diameter Zn rod.

explore the effect of hydrostatic pressure, and hence c/a ratio on the plastic behavior of hcp metals.

II. METHODS

A. High-pressure experiments

We deformed polycrystalline Zn, relying on hydrostatic pressure to tune the Zn c/a ratio, and performed experiments in regimes where $\{10\bar{1}2\}$ twins should be compressive (i.e., when $c/a > \sqrt{3}$), tensile (i.e., when $c/a < \sqrt{3}$), or at the transition between both regimes (i.e., when $c/a \approx \sqrt{3}$) (Fig. 1). In all cases, the initial material for this study is high-purity Zn wire (99.95 to 99.999%) of 0.5 mm (runs D1651, D1653, D1782) and 2 mm (Run Zn01) diameter, cut to a length of 0.8 mm (runs D1651, D1653, D1782) or 2.8 mm (Run Zn01). Deformation experiments were performed using the D-DIA multi-anvil apparatus installed at beam line 13-BM-D of the Advanced Photon Source (APS) at Argonne National Laboratory (runs D1651, D1653, D1782) [18] and at the ID06-LVP beam line of the European Synchrotron Radiation Facility (ESRF), Grenoble, France (run Zn01) [19]. The D-DIA setup consists of three pairs of mutually perpendicular anvils, with square tips of 6 mm for run Zn01, 3 mm for runs D1651 and D1653, and 2 mm for run D1782 (Fig. 2). The two vertical anvils are fixed to lower and upper guide blocks, while the other two pairs of wedge-shaped thrust anvils are in the horizontal plane and at 90° to each other. Hydrostatic pressure was increased by simultaneously advancing the horizontal and vertical rams over approximately two hours. Lateral and vertical anvils were then moved separately to induce deviatoric stresses, resulting in plastic sample deformation. Axial compression (sample shortening) was achieved by advancing the two vertical rams and retracting the four lateral anvils, while lateral compression (sample lengthening) was achieved by retracting the two vertical rams and advancing the four lateral anvils.

Monochromatic x-ray radiographs and diffractions were taken alternatively during the sample cycling in order to follow, *in situ*, the applied macroscopic strain, lattice strains (a marker of differential stress), and texture (Fig. 2). The high-pressure cell is relatively transparent to x rays along the beam path. Polycrystalline diamond anvils were used on the downstream side in order to allow for full collection of monochromatic powder diffraction rings. At both ESRF and APS, the sample x-ray transmission images were collected using a mm-sized beam, an yttrium-aluminum-garnet (YAG) scintillator to convert x rays to visible light, and a charge coupled device (CCD) camera. The exposure time for imaging was typically 1 second. The absorption contrast provided by the gold sheets at the top and bottom of the sample allowed measurement of the sample length, which was then converted to strain. At APS, we used a monochromatic beam ($\lambda = 0.1907$ Å, $E = 60$ keV) collimated to 200×200 mm^2 to obtain diffraction from the Zn sample. The diffraction images were recorded with a CCD detector with 2048×2048 pixels (pixel size of 0.079 mm) for 200 (run D1782) or 300 (runs D1651 and D1653) seconds. The detector tilt and rotation were calibrated against a CeO$_2$ standard. The sample-detector distance was refined from the ambient pressure diffraction on the sample (402.946 mm for run D1653, 402.689 mm

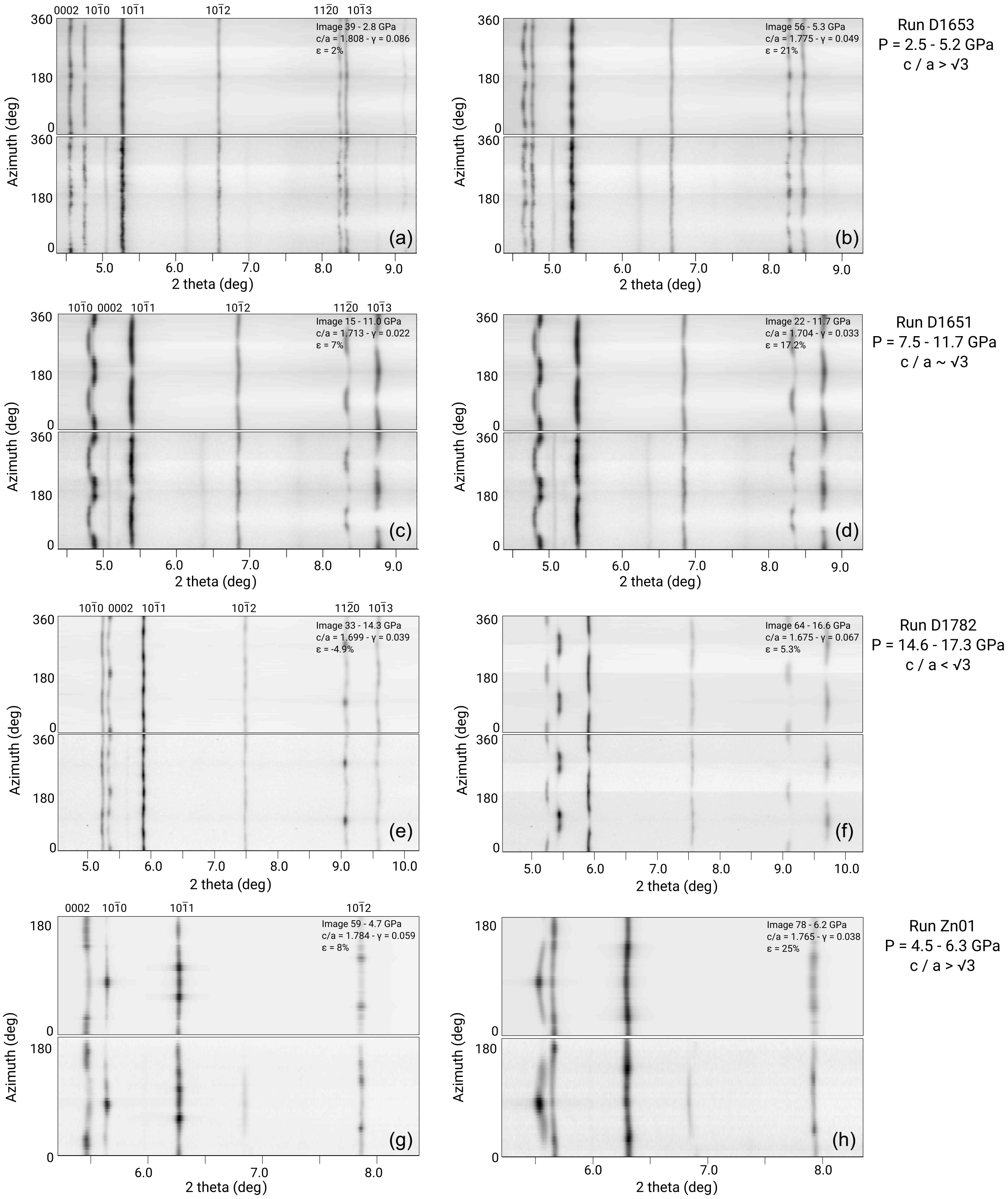

FIG. 3. Representative x-ray diffraction images and MAUD reconstructions for runs (a),(b) D1653, (c),(d) D1651, (e),(f) D1782, and (g),(h) Zn01. For each, the experimental diffraction intensities and MAUD reconstructions are plotted as a function of the diffraction angle 2θ and azimuth η in the bottom and upper panels, respectively. For each experiment, the figure shows diffraction images (a),(c),(e),(g) before starting a cycle of compression and (b),(d),(f),(h) at the end of the compression cycle. Laue indices of the hcp-Zn diffraction lines are indicated for each figure. Variations of diffraction intensities and positions with azimuth η are related to sample texture and strain, respectively.

for run D1653, and 403.351 mm for run D1782). At ESRF (run Zn01), we used a monochromatic beam ($\lambda = 0.2254$ Å, $E = 55$ keV) of c.a. $0.5 \times 0.5\,\text{mm}^2$ to obtain diffraction from the Zn sample. The diffraction images were recorded with a linear detector from DT Technology Co. made of 1536 pixels of 0.2 mm and rotated in the plane perpendicular to the direct beam in order to acquire multi-one-dimensional diffractions that were then rebuilt into 2D diffraction patterns (see details in Ref. [19]). The detector tilt and rotation were calibrated against a LaB_6 standard. The sample-to-detector distance was refined from the ambient pressure diffraction on the sample (2054.172 mm for run Zn01). Representative diffraction images of Zn at various pressures are shown in Fig. 3 and all raw diffraction images are provided online.

In all experiments, the sample was deformed at nearly constant pressure, in alternating cycles of axial compression

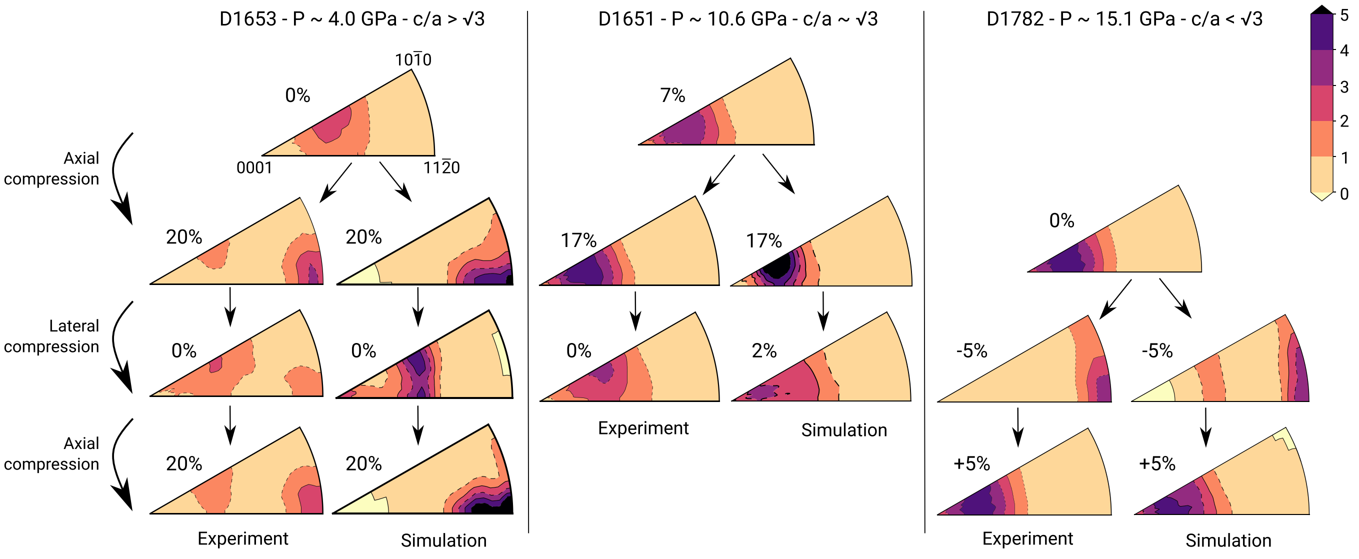

FIG. 4. Experimental (left columns) and EVPSC simulated (right columns) texture results shown as inverse pole figures of the deformation direction for experiments D1653 (left panel), D1651 (middle panel), and D1782 (right panel). The figure shows the texture evolution as a function of axial and lateral compression. The corresponding total macroscopic strain at which the texture was either measured or modeled is shown for each panel. Note that in order to have positive hydrostatic pressures, compressive strains are set positive and tensile strains are set negative.

(sample shortening) and lateral compression (sample lengthening), in order to study the effect of the active plastic deformation mechanism on sample texture (Figs. 4 and 10) and lattice strains (Figs. 5–7 and 11). While the experiment is intended to run at constant pressure, it was difficult to do so while introducing differential forces in the axial and

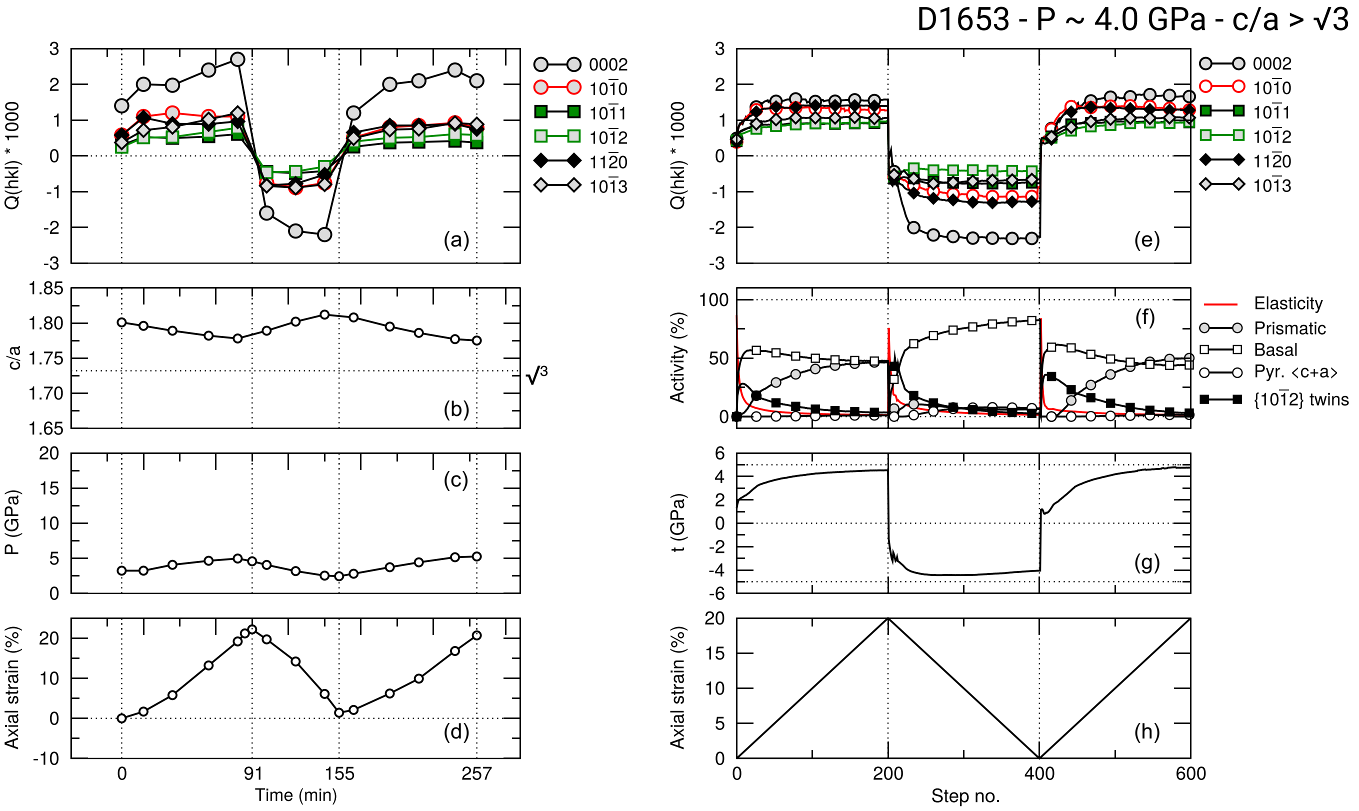

FIG. 5. Results for (a)–(d) experiment D1653 vs time and (e)–(h) EVPSC models vs step number. (a),(e) Measured and simulated lattice strain parameters $Q^{hkl}_{(t,S_{ijkl})}$, (b) Zn c/a ratio, (c) pressure, and (d) total applied strain vs time, deduced from x-ray radiography and diffraction measurements. Modeled (f) elastic and plastic strain accommodation, (g) differential stress, and (h) imposed axial strain as a function of step number in the simulation.

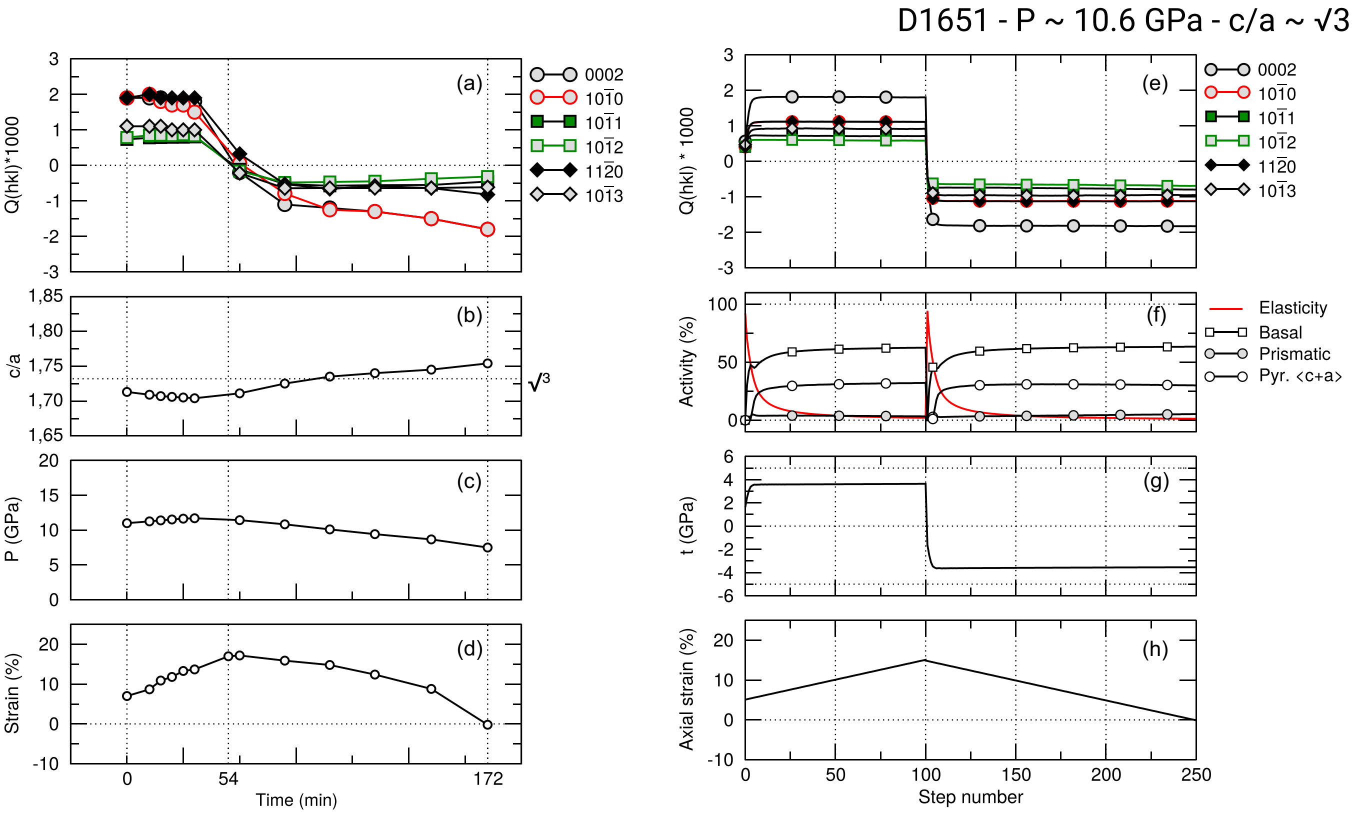

FIG. 6. Results for (a)–(d) experiment D1651 vs time and (e)–(h) EVPSC models vs step number.

lateral directions. Pressure was hence reevaluated for each diffraction image, based on the measured unit cell volume and the equation of state for Zn at high pressure [11].

Experiment D1653 was performed at pressures of 2.5–5.2 GPa, translating into c/a ratios of 1.775–1.790 (Fig. 1) with the sample deformed in axial compression up to 22% total axial strain in 91 min, lateral compression bringing back the sample to 1.5% total axial strain in 54 min, followed by axial compression up to 21% total axial strain in 102 min (Fig. 5). Experiment D1651 was performed at 7.5–11.7 GPa, translating into c/a ratios of 1.704–1.765. During pressure increase, the sample was submitted to approximately 7% axial compressive strain. It is further shortened to 17% total axial strain in 54 min and then laterally compressed back to 0% total axial strain in 123 min (Fig. 6). Experiment D1782 was performed at pressures of 14.6–17.3 GPa, translating into c/a ratios of 1.675–1.706. The sample was first laterally compressed down to −5% in 64 min and then compressed axially up to 5.6% total axial strain in 127 min (Fig. 7). Finally, experiment Zn01 was performed at pressures 4.5–6.2 GPa, translating into ratios of 1.764–1.786 with the sample deformed in axial compression up to 20% total axial strain in 135 min, lateral compression back to 7.5% total axial strain in 115 min, and, again, axial compression up to 25% total axial strain in 81 min (Fig. 11).

B. Analysis of high-pressure data

Diffraction images are analyzed using the Rietveld method and the software MAUD, which fit the diffraction profiles while minimizing the difference between the experimental observation and a model [20] following the general workflow described in Ref. [21]. Here, MAUD is used to extract the hydrostatic unit cell parameters of Zn (and, hence, the c/a ratio), the effect of stress derived from measured lattice strain parameters, and the sample texture. Diffraction images for runs D1651, D153, and D1782 show data from the 0002, $10\bar{1}0$, $10\bar{1}1$, $10\bar{1}2$, $11\bar{2}0$, and $10\bar{1}3$ reflections of Zn, while that of run Zn01 show data for 0002, $10\bar{1}0$, $10\bar{1}1$, and $10\bar{1}2$ (Fig. 3).

The diffraction images show systematic variations in intensity along diffraction rings, representative of sample texture. They are fitted using an orientation distribution function (ODF) computed using the extended Williams-Imhof-Matthies-Vinel (E-WIMV) algorithm implemented in MAUD assuming cylindrical symmetry about the compression direction. Extruded wires have cylindrical symmetry to start with and axial tension or compression do preserve the cylindrical symmetry about the compression axis. Textures are compactly represented with an inverse pole figure (IPF) of the deformation direction (Figs. 4 and 10). IPFs show the relation between the deformation direction and the crystal axes. Pole densities in the IPF are expressed in multiples of random distribution (m.r.d.), where an m.r.d. of 1 corresponds to a random distribution. In the case of a perfectly oriented sample or a single crystal, the m.r.d. would be equal to infinity at the orientation of compression axis with respect to the crystal, and zero elsewhere.

The diffraction images also show systematic variations in peak positions with azimuth for each diffraction ring. The

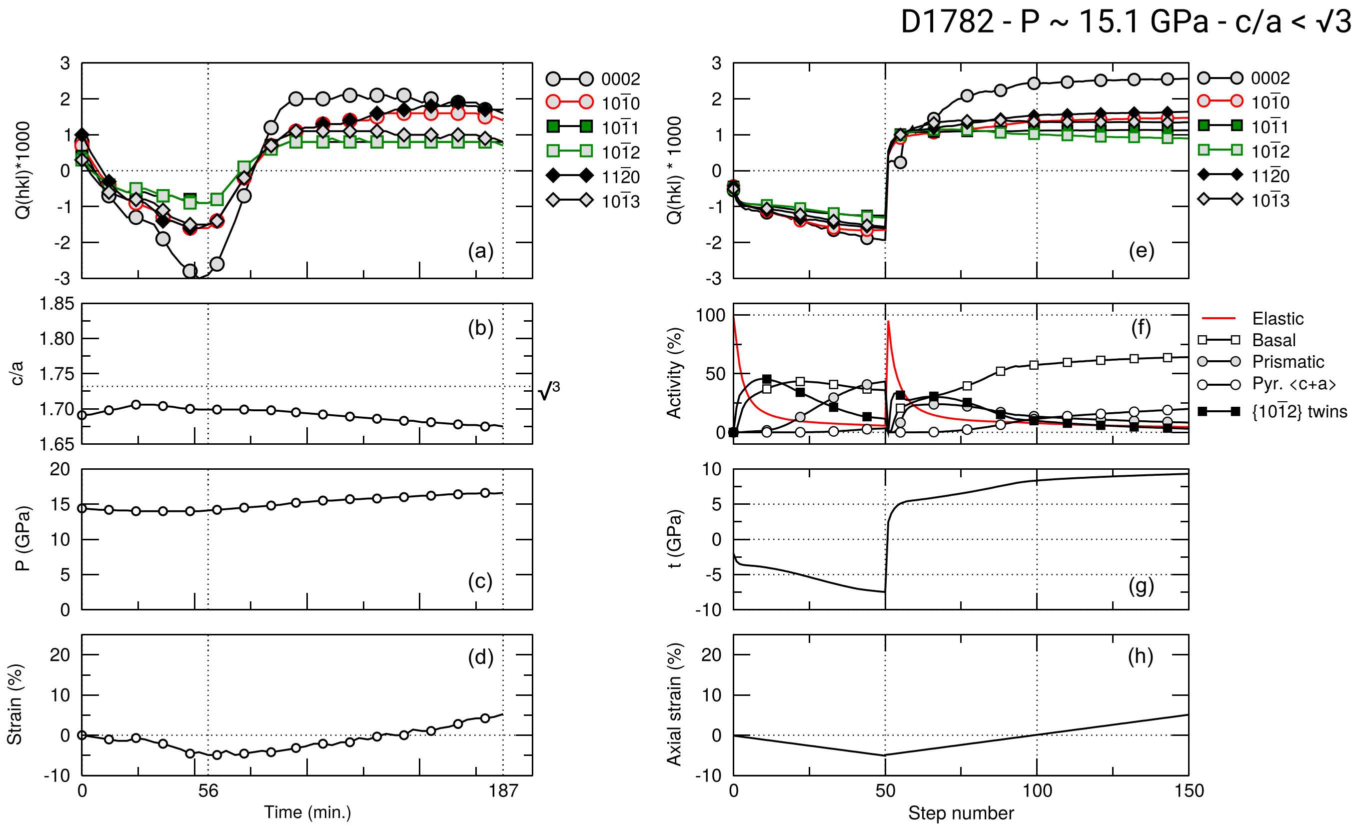

FIG. 7. Results for (a)–(d) experiment D1782 vs time and (e)–(h) EVPSC models vs step number.

position of each diffraction ring and its azimuth dependence are a function of both the hydrostatic unit cell parameters of Zn, a and c, and of the deviatoric stress applied to the sample. The macroscopic stress in axial D-DIA experiments is usually expressed as a sum of the hydrostatic and deviatoric components,

$$\sigma_{ij} = \sigma_P \delta_{ij} + \sigma'_{ij} = \begin{bmatrix} \sigma_P & 0 & 0 \\ 0 & \sigma_P & 0 \\ 0 & 0 & \sigma_P \end{bmatrix} + \begin{bmatrix} -\frac{t}{3} & 0 & 0 \\ 0 & -\frac{t}{3} & 0 \\ 0 & 0 & \frac{2t}{3} \end{bmatrix}, \tag{3}$$

where σ_P is the hydrostatic pressure and t the differential stress. Under the assumption of isostrain (Voigt) or isostress (Reuss) bounds, the effect of differential stress on the measured d-spacings could be expressed as [22,23]

$$\epsilon^{hkl}_{(\psi)} = \frac{d^{hkl,m}_{(\psi)} - d^{hkl,P}}{d^{hkl,P}} = Q^{hkl}_{(t,S_{ijkl})}(1 - 3\cos^2\psi), \tag{4}$$

where $d^{hkl,P}$ is the lattice spacing of the hkl planes under the hydrostatic pressure σ_P and can be calculated from the unit cell parameters a and c and the Laue indices of the diffraction line, $d^{hkl,m}_{(\psi)}$ is the lattice spacing measured when a deviatoric component is superimposed, and ψ is the angle between the diffracting plane normal and the axial stress direction. $Q^{hkl}_{(t,S_{ijkl})}$ is called the lattice strain parameter. Under the Voigt or Reuss bounds, $Q^{hkl}_{(t,S_{ijkl})}$ is only a function of the differential stress t and the elastic compliances of the single crystal [22,23]. Reuss and Voigt assumptions fail in materials undergoing plastic deformation, in which stress can be heterogeneous and depend on each individual grain history. In such a case, the relationship between $Q^{hkl}_{(t,S_{ijkl})}$, t, and the elastic compliances derived under the Reuss or Voigt assumption does not truly capture the sample stress state [24]. Nevertheless, experience has shown that using lattice parameters and the equation above to express diffraction data from high-pressure axial deformation experiments is relevant as a measure of the evolution of internal elastic strains to be compared with the same data predicted by more advanced micromechanical modeling [25–27].

In this work, MAUD is hence used to extract the hydrostatic unit cell parameters of Zn, a and c, and lattice strain parameters $Q^{hkl}_{(t,S_{ijkl})}$ for each available diffraction line, as implemented in the so-called "radial diffraction in the diamond anvil cell (DAC)" strain model. The hydrostatic unit cell parameters of a and c are then used to estimate the Zn c/a ratio as well at its unit cell volume, from which we evaluate the hydrostatic pressure σ_P using the equation of state of Zn [11]. Lattice strains, c/a ratios, hydrostatic pressures, and total axial strains for all runs and all data points are presented in Figs. 5–7 and 11.

C. EVPSC modeling and plastic mechanisms

The shear activity on the basal, prismatic, and pyramidal slip systems, in addition to that of the $\{10\bar{1}2\}$ twinning mode, has two relevant effects: (i) it determines the texture evolution during cycling and, (ii) because plasticity relaxes internal stresses, it controls the evolution of internal elastic strains. As a consequence, the characteristics of the internal strain evolution, expressed using the lattice strain parameters $Q^{hkl}_{(t,S_{ijkl})}$

in the experimental data, depend on the deformation modes being activated. The comparison of predicted and measured texture and internal strains hence provides an indirect way to identify the active deformation modes at a given pressure, the associated threshold stress or critical resolved shear stress (CRSS), and their relative contribution to crystallographic shear. This can be performed using elastoviscoplastic self-consistent (EVPSC) models.

Deformation experiments in the D-DIA do not provide direct stress tensors as in typical deformation experiments. Hence, the macroscopic stress-strain curves are not readily available from such experiment. As such, it can be difficult to adjust complex hardening laws for each slip and twinning mode, as is routinely done in ambient condition experiments [28,29]. As a consequence, and in order not to introduce more parameters than necessary, the threshold stress of each deformation mode was kept constant during the EVPSC simulations. The experimentally measured internal elastic strains, expressed through the lattice strain parameters $Q^{hkl}_{(t,S_{ijkl})}$, are kept bounded by the plastic relaxation mechanisms and are used as guidance to adjust the CRSS of slip and twinning systems.

For the mechanical simulations, we use the EVPSC model of Ref. [30], coupled with the predominant twin reorientation (PTR) model [31], to simulate the twinning reorientation and its contribution to texture. In a nutshell, the model is based on representing the aggregate by a collection of crystal orientations (grains) with weights (volume fractions) selected to reproduce the initial texture. Each grain is treated as an ellipsoidal inclusion embedded in—and interacting with—a homogeneous effective medium (HEM) which represents the polycrystal. Grains and HEM are treated as anisotropic elastoplastic entities, obeying constitutive laws:

$$\dot{\varepsilon}^{(g)} = M^{(g),\mathrm{el}} : \dot{\sigma}^{(g)} + M^{(g),\mathrm{vp}} : \sigma^{(g)} + \dot{\epsilon}_0^{(g)}, \tag{5}$$

$$\dot{\bar{\varepsilon}} = \overline{M}^{\mathrm{el}} : \dot{\bar{\sigma}} + \overline{M}^{\mathrm{vp}} : \sigma + \dot{\bar{\varepsilon}}_0. \tag{6}$$

Here, $\sigma^{(g)}$, $\dot{\varepsilon}^{(g)}$, and $\dot{\epsilon}_0^{(g)}$ are the stress, strain rate, and back-extrapolated strain rate in each grain, and $M^{(g),\mathrm{el}}$ and $M^{(g),\mathrm{vp}}$ are the grain elastic and viscoplastic compliances, respectively. The magnitudes with bars in Eq. (6) are the equivalent magnitudes for the HEM. The viscoplastic compliance of the grain is given by a power law,

$$M_{ijkl}^{(g),\mathrm{vp}} = n\dot{\gamma}_0 \sum_s \frac{m_{ij}^s m_{kl}^s}{\tau^s} \left(\frac{m^s : \sigma^{(g)}}{\tau^s} \right)^{n-1}, \tag{7}$$

where $\dot{\gamma}_0$ is a reference shear strain rate, τ^s the CRSS of the deformation mode system s, m^s is its symmetric Schmid factor, and n (typically, $n = 20$) is an empirical parameter associated with rate sensitivity. For exclusively elastic (or exclusively viscoplastic) behavior, the grain strain rate and stress rate (or strain rate and stress) are related to the corresponding values for the HEM via the interaction equation, which couples the stress and strain rate in grains and medium. For an elastoviscoplastic medium, Ref. [30] adopted the assumption that the total strain rates are related by a linear superposition of the purely elastic and the purely viscoplastic interaction equations [32],

$$(\dot{\bar{\varepsilon}} - \dot{\varepsilon}^{(g)}) = -\widetilde{M}^{\mathrm{el}} : (\dot{\bar{\sigma}} - \dot{\sigma}^{(g)}) - \widetilde{M}^{\mathrm{vp}} : (\bar{\sigma} - \sigma^{(g)}). \tag{8}$$

The interaction tensors $\widetilde{M}^{\mathrm{el}}$ and $\widetilde{M}^{\mathrm{vp}}$ are a function of the elastic and viscoplastic HEM moduli and the Eshelby tensors S^{el}andS^{vp}, as

$$\widetilde{M}^{\mathrm{el}} = (I - S^{\mathrm{el}})^{-1} : S^{\mathrm{el}} : \overline{M}^{\mathrm{el}}, \tag{9}$$

$$\widetilde{M}^{\mathrm{vp}} = (I - S^{\mathrm{vp}})^{-1} : S^{\mathrm{vp}} : \overline{M}^{\mathrm{vp}}. \tag{10}$$

At each deformation step, the macroscopic moduli $\overline{M}^{\mathrm{el}}$ and $\overline{M}^{\mathrm{vp}}$ are obtained self-consistently by enforcing the condition that the average stress and strain rate over the grains coincides with the stress and strain rate applied on the polycrystal,

$$\bar{\sigma} = \langle \sigma^{(g)} \rangle \quad \text{and} \quad \dot{\bar{\varepsilon}} = \langle \dot{\epsilon}^{(g)} \rangle. \tag{11}$$

The model provides the evolution of crystallographic orientation and of stress in each grain, from which the texture and the internal strain evolution can be predicted and compared with the experimental measurements.

The modeling of twinning follows the PTR model, based on replacing a current orientation (parent) by the twin related (child) orientation when certain conditions are met. Such approach is statistically meaningful when the number of grains used to represent the aggregate is large. Within PTR, as deformation is incrementally imposed onto the aggregate, one keeps track of the accumulated shear strain $\gamma^{t,g}$ contributed by each twin system t in each grain g, and of the associated volume fraction $v^{t,g} = \frac{\gamma^{t,g}}{S^t}$ in the grain (S^t is the characteristic twin shear). The weighted sum of $v^{t,g}$ over all grains and over all twin variants belonging to a given twin mode represents the *accumulated twin fraction* in the aggregate for the particular twin mode [the one that one would extract from an electron backscatter diffraction (EBSD) image],

$$V^{\mathrm{acc,t\text{-}mode}} = \sum_g \sum_t \frac{\gamma^{t,g}}{S^t} w^g. \tag{12}$$

The total volume associated with the fully reoriented grains for that mode is called the *effective twinned fraction*$V^{\mathrm{eff,t\text{-}mode}}$,

$$V^{\mathrm{eff,t\text{-}mode}} = \sum_g w^{g,\mathrm{reoriented}}. \tag{13}$$

In order to keep the $V^{\mathrm{acc,t\text{-}mode}}$ and $V^{\mathrm{eff,t\text{-}mode}}$ consistent, a threshold volume fraction $V^{\mathrm{th,t\text{-}mode}}$ is defined,

$$V^{\mathrm{th,t\text{-}mode}} = A^{\mathrm{th1}} + A^{\mathrm{th2}} \frac{V^{\mathrm{eff,t\text{-}mode}}}{V^{\mathrm{acc,t\text{-}mode}}}. \tag{14}$$

At the end of each incremental step, some grains are fully reoriented by twinning according to the following procedure: grains are picked at random from the whole set of orientations, and the twin system having accumulated the maximum volume fraction in the grain is identified. If the volume fraction exceeds $V^{\mathrm{th,t\text{-}mode}}$, the grain is reoriented by twinning and its volume fraction is added to $V^{\mathrm{eff,t\text{-}mode}}$. As more grains are fully reoriented by twinning, $V^{\mathrm{eff,t\text{-}mode}}$ increases and so does the threshold defined by Eq. (14). The process is repeated until either all grains are randomly checked or until the effective twin volume exceeds the accumulated twin volume, whichever comes first. In the latter case, we stop reorientation by twinning and proceed to the next deformation step. A characteristic of this process is that the twinned fraction is consistent with the amount of shear that the twins contribute to deformation.

The algorithm delays grain reorientation by twinning until a minimum volume fraction of twinning, A^{th1}, is accumulated in any given system. A large value of the parameter A^{th2} has the effect of slowing down the rate of twin reorientation. The texture evolution due to twin reorientation is weakly dependent on the precise values of A^{th1} and A^{th2} [33]. In the current simulations, we use $A^{\mathrm{th1}} = 0.10$ for the lower threshold and $A^{\mathrm{th2}} = 0.5$ for the upper threshold. The twinned grain is treated as a new grain without previous twin history, and upon load reversals, it may undergo reorientation by twinning, which effectively amounts to detwinning.

III. RESULTS

A. Diffraction

Representative diffraction images and MAUD reconstructions are presented in Fig. 3. In all cases, diffraction lines of Zn are clearly visible and well reproduced by the MAUD analysis.

At low pressures, when $c/a > \sqrt{3}$ (runs D1653 and Zn01), the 0002 diffraction line appears at smaller diffraction angles than that of $10\bar{1}0$. When $c/a \approx \sqrt{3}$ (run D1651), 0002 and $10\bar{1}0$ overlap. And when $c/a < \sqrt{3}$ (run D1782), 0002 appears at larger diffraction angles than $10\bar{1}0$. Thanks to the redundant information between diffraction lines, texture can be fit properly for all cases. Lattice strain parameters for run D1651, however, may be somewhat biased due to the overlap of the 0002 and $10\bar{1}0$ peaks.

Runs D1653 and Zn01 were performed at similar pressures. However, the textures are sharper and lattice strains noisier in run Zn01 compared to run D1653. The may be due to a larger grain size and sample diameter in run Zn01. In addition, the average pressure in run Zn01 is larger than that of run D1653 and the experiment is therefore less representative of the "low-pressure" behavior. The results of run Zn01 are hence presented in Figs. 10 and 11 and will not be discussed or modeled in great detail in this paper. They are broadly consistent with those of run D1653, regarding textures, lattice strains, and micromechanical modeling. This confirms the findings of run D1653 and what will be described in the rest of the paper.

B. Deformation textures

At low pressures, when $c/a > \sqrt{3}$, axial compression (sample shortening) induces a re-orientation of Zn grains so that their c axes are perpendicular to the compression axis (run 1653, Fig. 4). Upon lateral compression (sample lengthening) the c axes rotate by nearly 90° and form a maximum at approximately 30° away from 0001 in the IPF. This texture is reversed when the sample is again set to compression, again reorienting the c axes of Zn in a direction perpendicular to compression. Results for run Zn01 (Fig. 10), performed over a similar pressure range, are similar, with the c axes of Zn becoming perpendicular (parallel) to the direction of deformation in axial compression (lateral compression). Whether sample lengthening induces a pure 0001 texture (run Zn01) or a maximum 30° away from 0001 (run D1653) depends on the starting sample texture.

At intermediate pressures, when $c/a \approx \sqrt{3}$ (run 1651, Fig. 4), the IPF maximum does not significantly shift upon cycles of axial/lateral compression, with a maximum at ∼30° away from 0001 in the IPF. Texture strength, on the other hand, depends on the style of deformation, increasing upon cycles of axial compression and decreasing during lateral compression.

Finally, at higher pressures, when $c/a < \sqrt{3}$ (run D1782, Fig. 4), texture observations are reversed relative to the low-pressure case, with a maximum near 0001 obtained upon axial compression. Upon lateral compression, the c axes rotate 90° away from the deformation direction, forming a maximum at $10\bar{1}0$ in the IPF.

In connection with the texture variations observed during loading and reversals, we will demonstrate, in what follows, that {10$\bar{1}$2} compression twinning and detwinning control texture evolution at low pressure, {10$\bar{1}$2} tensile twinning and detwinning are dominant at high pressure, and slip activity only can explain this texture evolution at intermediate pressure.

C. Strains, pressure, and lattice parameters

Lattice strains, c/a ratios, hydrostatic pressures, and total axial strains for all runs and all data points are presented in Figs. 5–7 and 11. The figures confirm the target pressure ranges for all four experiments, i.e., pressure region where $c/a > \sqrt{3}$ for runs D1653 and Zn01, $c/a \approx \sqrt{3}$ for run D1651, and $c/a < \sqrt{3}$ for run D1782.

The D-DIA experiment generates deformation by moving lateral and vertical anvils independently. In this process, it is difficult to maintain a truly constant sample volume and hence hydrostatic pressure [Figs. 5(c), 6(c), 7(c), 11(c)]. In run D1653, pressure ranges from 2.5 to 5.3 GPa, with a mean pressure of 4.0 GPa. In run Zn01, pressure ranges from 4.5 to 6.3 GPa, with a mean pressure of 5.2 GPa. In run D1651, pressure ranges from 7.5 to 11.7 GPa, with a mean pressure of 10.6 GPa. Finally, in run D1782, pressure ranges from 14.0 to 16.6 GPa, with a mean pressure of 15.1 GPa.

Lattice strain parameters increase up to 3×10^{-3} upon axial compression and decrease down to -3×10^{-3} upon lateral compression. In most cases, the measured lattice strains for the 0002 reflections, originating from basal plane families, are larger than those of other peaks. This is partly because the crystal stiffness C_{33} is about half $C_{11} = C_{22}$ within the tested pressure interval (see Table I). The smallest lattice strains are observed for reflections corresponding to pyramidal plane families, either $10\bar{1}1$ or $10\bar{1}2$, and lattice strains for reflections corresponding to prismatic plane families, such as $10\bar{1}0$ and $11\bar{2}0$, lead to intermediate values. Experiment D1651 does differ from other runs, with the lattice strains for 0002 and $10\bar{1}0$ of the same magnitude. Do note, however, that both 0002 and $10\bar{1}0$ diffraction peaks overlap in this pressure range [Figs. 3(c) and 3(d)] and the fitting of lattice strains for those peaks in MAUD may be inconsistent.

TABLE I. Elastic moduli of Zn used in the EVPSC modeling of experiments D1653, D1651, and D1782 (from Ref. [17]). Units of GPa.

P	C_{11}	C_{33}	C_{12}	C_{13}	C_{44}	C_{66}
4.0	204	93	48	60	45	78
10.6	262	138	65	80	61	97
15.1	299	167	76	90	71	109

In a plastically deforming material, lattice strains themselves cannot be directly interpreted. They can be used, however, to calibrate polycrystal calculations with self-consistent plasticity models, as we will describe in the next section.

D. EVPSC modeling of the experimental data

The simulations of texture evolution depend on the plastic system activity and are not sensitive to the elastic properties of the crystal. The evolution of internal strain in grains, however, is sensitive to both the elastic constants and the threshold stress assigned to slip and twin systems. We hence use the elastic constants obtained by density functional theory (DFT) simulations [17] at a fixed average pressure in each run (Table I). Pressure variations during each run are not accounted for.

We adjust the active deformation modes and their threshold stress τ^s in order to best reproduce the experimentally measured textures and lattice strain parameters vs strain. The test conditions prevent us from extracting a true stress-strain response as the differential stress t [Eq. (3)] is not directly measured in the experiment, but deduced from the EVPSC modeling. As a consequence, the conservative approach is taken of keeping the threshold stress τ^s constant in Eq. (7) for each slip and twin systems throughout deformation (Table II). Hardening models with strain-dependent threshold stresses to account for deformation hardening are available in our EVPSC implementation but, at this point, their use would be an overinterpretation of the experimental data. Table II lists the deformation modes and their threshold stresses adjusted to the experimental data for low-, intermediate-, and high-pressure conditions.

1. Low-pressure experiment, $c/a > \sqrt{3}$

In run D1653, the first compression stage to 20% axial strain induces a large reorientation that aligns the $\langle 11\bar{2}0\rangle$ directions of Zn with the load axis (Fig. 4). Such a drastic reorientation of hcp grains during deformation is consistent with a twinning mechanism which can generate new grain orientations at near 90° of the parent grain. Simulations confirm that the latter effect comes from compressive $\{10\bar{1}2\}$ twin activity (Fig. 4). The initial texture aligns the crystal's c axes with compression. Compressive twinning is then triggered upon sample compression.

The second tensile stage of 20% reverses the strain, lengthening the sample, and induces detwinning on the texture component at $11\bar{2}0$ in the IPF, making it disappear. Finally, a third compressive stage to 20% reactivates twinning and regenerates the $11\bar{2}0$ component. The simulations indicate that twinning is active in all three stages (Fig. 5) and is responsible for most of the observed texture evolution (Fig. 4).

Basal, prism, and pyramidal slip, however, exhibit non-negligible activity throughout as well, and their relative activity depends on how the main texture component is oriented with respect to the compressive or tensile axis. Their relative threshold stresses, however, are difficult to set based on texture alone. At this stage, we resort to investigate the experimental and modeled lattice strain parameters. Dominant active slip systems affect the ordering of lattice strain parameters, while the absolute threshold stresses τ^S control the lattice strain amplitude. A remarkable match can be obtained with the absolute threshold stresses τ^S provided in Table II (Fig. 5). The EVPSC simulations reproduce remarkably well the experimental counterpart for all diffraction families, and further support the CRSS values assigned to the deformation systems.

TABLE II. CRSS of the plastic deformation modes extracted from the EVPSC models (units of MPa). $\{10\bar{1}2\}$ twinning is disabled for the modeling of run D1651.

Experiment	$\{0001\}$ basal slip	$\{10\bar{1}0\}$ prismatic slip	$\{10\bar{1}1\}$ pyramidal slip	$\{10\bar{1}2\}$ twinning
D1653, 4.0 GPa	40	250	400	50
D1651, 10.6 GPa	90	250	250	
D1782, 15.1 GPa	250	500	1000	200

2. Intermediate-pressure experiment, $c/a \sim \sqrt{3}$

Run D1651, corresponding to a pressure in the range of 10.5 GPa, is likely the most interesting to analyze because, with the corresponding value of the c/a ratio, the characteristic shear of $\{10\bar{1}2\}$ twins is null or close to null. Under such condition, the twin volume fraction involved in accommodating even a modest shear would involve the whole grain volume.

Deformation textures show that the near 90° grain, reorientation induced by $\{10\bar{1}2\}$ twins is not observed in the experiment as the maximum in the IPF remains in the vicinity of 0001, whatever the cycle of axial or lateral compression (Fig. 4). The combined simulations of textures and lattice strain parameters for this test (Figs. 4 and 6) are consistent with the absence of twinning, mostly basal and pyramidal $\langle c+a\rangle$ slip activity, and a very small contribution of prismatic slip. The grain rotation is reversed upon reversing the axial and lateral compression because shear reversions occur on the same systems during both stages of deformation.

The quantitative comparison between simulation and experiment is not as good as for run D1653, but remains fair, with a good modeling of the amplitude and order of lattice strain parameters, apart from those for the $10\bar{1}0$ reflection which, as explained previously, overlaps with 0002 in the experimental data and may not be fitted properly. In addition, the lack of dislocation hardening in the model is likely to introduce more significant effects in this case, where all deformation is accommodated via slip.

3. *High-pressure experiment, $c/a < \sqrt{3}$*

Deformation in run D1782 at ~15.1 GPa pressure reveals the consequence of the anomalous effect of pressure on twinning in Zn. For the c/a ratio associated with this pressure, $\{10\bar{1}2\}$ twins should be tensile, i.e., activated when the Zn c axes are under a tensile stress (Fig. 1).

In this experiment, the first loading stage was a lateral compression, up to 5% strain, and the second stage was 10% compressive, namely, a full reversal plus an extra 5% compressive strain. The observed textures confirm the "androgynous" character of the $\{10\bar{1}2\}$ twin in Zn (Fig. 4). In fact, lateral compression induces tension along the c axis and activates tensile twinning for this initial texture, which reorients the c axes by about 90° and creates twinned domains, where the $\langle 11\bar{2}0\rangle$ directions are aligned with the axial tensile direction. Reversing the applied strain to compression induces tensile stresses along the c axis of those reoriented grains, which then activates the $\{10\bar{1}2\}$ twin and reverts to the original texture. Past such point, the rest of the deformation is accommodated by prismatic, basal, and pyramidal slip, and the texture does not show any further substantial change.

At this stage, and as for the other runs, we optimize the absolute threshold stresses τ^S for each active slip and twinning system in order to match the lattice strains measured experimentally. Despite keeping it constant, remarkable match can be obtained with the absolute threshold stresses τ^S provided in Table II (Fig. 7).

IV. DISCUSSION

A. The androgynous $\{10\bar{1}2\}$ twin in Zn

The measurements of runs D1653 and D1782, performed at pressures ranges where $c/a > \sqrt{3}$ and $c/a < \sqrt{3}$, respectively, do confirm the androgynous nature of $\{10\bar{1}2\}$ twins in hcp-Zn. In addition, our experiments show that those twins behave the same as twins activated under normal pressure conditions, including the important mechanism of detwinning upon stress reversals.

Below ~10 GPa, $c/a > \sqrt{3}$ and $\{10\bar{1}2\}$ twins are compressive, i.e., they activate when the c axes of Zn are submitted to compressive stresses. In experiments with deformation in axial compression, $\{10\bar{1}2\}$ twins are activated in grains in the vicinity of 0001 in the IPF and reorient the grains to orientations near $11\bar{2}0$ or $10\bar{1}0$ [i.e., stages 1 and 3 in run D1653 (Fig. 4) and run Zn01 (Fig. 10)]. During cycles of lateral compression or sample lengthening, $\{10\bar{1}2\}$ twins are activated in grains near $11\bar{2}0$ or $10\bar{1}0$ in the IPF and generate new orientations near 0001 [i.e., stage 2 in run D1653 (Fig. 4) and run Zn01 (Fig. 10)].

Above ~10 GPa, $c/a < \sqrt{3}$ and $\{10\bar{1}2\}$ twins are tensile, i.e., they activate when the c axes of Zn are submitted to tensile stresses. In experiments with deformation in axial compression, $\{10\bar{1}2\}$ twins will be activated in grains with their c axes near 90° of the compression direction and for which the stresses applied to the c axis are tensile. This results in the formation of new orientations in the vicinity of 0001 in the IPF (i.e., cycle 2 for run D1782 in Fig. 4). When lateral compression or sample lengthening is applied, $\{10\bar{1}2\}$ twins are activated in grains with their c axes near the lengthening direction, i.e., near 0001 in the IPF, and generate new orientations near $11\bar{2}0$ or $10\bar{1}0$ in the IPF (i.e., cycle 1 for run D1782 in Fig. 4).

The androgynous nature of twinning in hcp metals was predicted on the basis of crystallography and the fact that contrary to slip, the Burgers vector of twins is not a lattice vector, but usually much smaller [5]. As a consequence, relatively small variations of c/a result in reversals of the twinning shear. The transition from tensile to compressive nature for $\{10\bar{1}2\}$ twins takes place at $c/a = \sqrt{3} \approx 1.732$, at $c/a = 1.5$ for $\{10\bar{1}1\}$ and $\{10\bar{1}3\}$ twins, and at $c/a = \sqrt{2} \approx 1.414$ for $\{11\bar{2}2\}$ and $\{11\bar{2}4\}$ twins. The transition from tensile to compressive nature of $\{10\bar{1}2\}$ twins in Zn was already inferred using diamond anvil cell experiments, increasing pressure from ambient to 25 GPa, showing little texture evolution below 10 GPa and a strengthening of a 0001 compression texture above 15 GPa [16]. Here, this transition is formally demonstrated by cycles of sample shortening and lengthening below and above the ~10 GPa transition pressure, and by corroborating the system activity via matching the experimental evolution of lattice strains.

B. What happens when $c/a \approx \sqrt{3}$?

Both texture and lattice strain analysis show that twinning is not active around 10 GPa. The mechanical behavior of the sample can be explained using a combination of mostly basal and pyramidal $\langle c + a\rangle$ slip activity, in addition to a very small contribution of prismatic slip.

The lack of twin activity in the vicinity of the 10 GPa pressure can be rationalized as follows. At low pressure, the directional twin shear can be activated by compression along the c axis, and at high pressure by tension along the c axis. In both cases, the driving force is a shear applied on the $(10\bar{1}2)$ twin plane, which displaces the atoms every two-atomic layers by one Burgers vector. For twinning to completely reorient the lattice, however, it is necessary that atoms in intermediate layers "shuffle" towards the perfect lattice positions.

Figure 8 shows dichromatic complexes associated with twinning on $\{10\bar{1}2\}$ for three different ratios of c/a. As pressure nears 10 GPa, the Burgers vector decreases to zero, but the direction of the atomic shuffles is nearly independent of the c/a value, larger than the Burgers vector in magnitude, and, in general, different from the direction of the shear vector. Performing such displacements requires the involved atoms to go over atomic energy barriers in order to reconstitute the lowest-energy state of the perfect lattice. The driving force comes from those atoms in the second layer that are being displaced by the shear to their equilibrium positions. In the vicinity of $c/a = \sqrt{3}$, however, twinning reorientation involves only pure shuffle and the displacement of the second-layer atoms is very small or null and incapable of driving the intermediate-layer atoms over the shuffle energy barrier. In addition, in the case of $\{10\bar{1}2\}$ twins, the number of atoms that have to be driven by shuffle is in a proportion of 3 to 1 with respect to the "driving" atoms displacing along the Burgers vector [5]. The previous arguments would explain why there is a c/a interval in which twinning is not active. However, one could still argue whether the difference in elastic energy

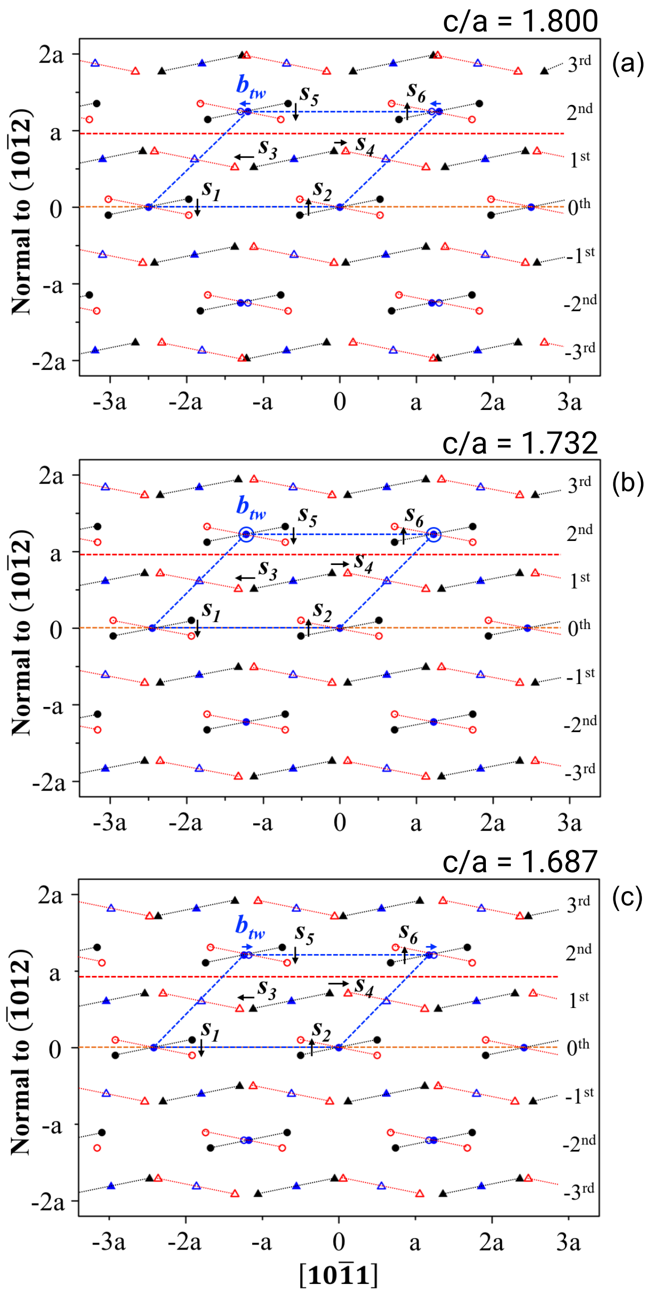

FIG. 8. Dichromatic diagrams showing atomic displacements associated with twinning on {10$\bar{1}$2} planes for $c/a = 1.8$ ($|\mathbf{b}_{\mathbf{tw}}| = -0.096a$), $c/a = 1.732$ ($|\mathbf{b}_{\mathbf{tw}}| = 0.0$), and $c/a = 1.687$ ($|\mathbf{b}_{\mathbf{tw}}| = 0.064a$), corresponding to compression twinning, pure shuffle, and tension twinning, respectively. Circles and triangles correspond to position along the [$\bar{1}2\bar{1}0$] direction (normal to picture). Dotted lines connect atom pairs with the lattice point in the middle. The orange dashed line represents the coherent twin boundary and the red dashed line the gliding plane. Within the elementary cell (enclosed by blue dashed lines), the Burgers vector of the twinning dislocation ($\mathbf{b}_{\mathbf{tw}}$) is defined as the difference between lattices in matrix and twin on the second layer. Shuffle vectors $\mathbf{S}_\mathbf{i}$ are defined after twinning dislocation shearing.

between the parent and the reoriented twinned domain can work in favor of the shuffling mechanism, even though the crystal reorientation would not provide any shear under the applied stress. In what follows, we show that the elastic energy of the twinned domain is larger and then such is not the case.

According to Table I, the Zn crystal is elastically very anisotropic and, under an externally applied stress, the elastic energy of a grain will be different from that of its twin-related orientation. In addition, since when $c/a = \sqrt{3}$ there is no plastic shear associated with twinning, there is no stress relaxation associated with the potential twin reorientation. In what follows, a quantitative evaluation of the elastic strain in parent and twin grains is performed. Since, in the case of {10$\bar{1}$2} twins, the c axis reorients by about 90°, two orientations are tagged in an aggregate formed by 500 random grains: grain no. 1 has the c axis parallel to x_3 and grain no. 2 has the c axis parallel to x_2. The EVPSC code described in Sec. II C is used to simulate axial compression along x_3. The elastic constants at 4, 10, and 15 GPa (Table I) are assumed, the strain imposed to the aggregate is $\epsilon_{33} = -10^{-3}$ (within the elastic range), and the elastic energy $\omega = \frac{1}{2}\sigma_{ij}\varepsilon_{ij}$ is computed for grains no. 1 and no. 2. The average compressive stresses in the aggregate are 111, 147, and 165 MPa when the elastic constants at 4, 10, and 15 GPa pressure are used, respectively. The elastic energy of grain no. 2 is always larger than the one of grain no. 1 by 18.0, 10.4, and 8.6%. This result is the same when a tensile stress is applied in the elastic regime. The corollary is that for a grain with the c axis aligned with the tensile or compressive loading, the elastic energy increases for all pressures in the twin-reoriented grain. The specific conclusion is that at ~10 GPa, where there is no transformation shear to induce stress relaxation, the elastic energy cannot be a driver for overcoming the energy required for atomic shuffling, and twin reorientation will not take place.

C. Other deformation mechanisms

Other active deformation mechanisms that we identify are the usual basal, prismatic, and pyramidal slips. In all cases, basal slip dominates the plastic activity [Figs. 5(f), 6(f), 7(f)]. The activity of those slip systems depends on pressure, i.e., the c/a ratio, and loading conditions.

Below 10 GPa, where $c/a > \sqrt{3}$, deformation in axial compression is controlled by basal slip, {10$\bar{1}$2} twinning, and a significant contribution of prismatic slip. In lateral compression, deformation is controlled by basal slip and {10$\bar{1}$2} twinning, with a minimal contribution of prismatic slip. The situation is reversed above 10 GPa, where $c/a < \sqrt{3}$, and for which deformation involves basal slip, {10$\bar{1}$2} twinning, and with prismatic slip mostly activated during lateral compression and only weakly active during axial compression.

This counterintuitive behavior of prismatic slip is related to sample texture. Comparing textures in Fig. 4 and slip system activities in Figs. 5(f) and 7(f), one realizes that prismatic slip activates after {10$\bar{1}$2} twins do, when most grains lie in the vicinity of 11$\bar{2}$0 in the IPF. In fact, under such conditions, prismatic slip is favored as many grains will lie at orientations with a high Schmid factor for at least one of the prismatic slip systems. On the contrary, when most grains lie near 0001 in the IPF, plasticity will be controlled by the much easier basal slip system, despite its very low Schmid factor, and generate

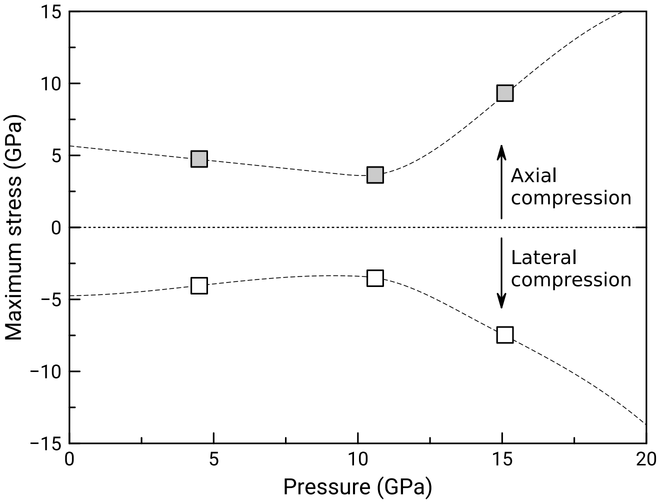

FIG. 9. Range of differential stress modeled in hcp-Zn during cycles of axial and lateral compression. Full and open squares are stresses modeled during axial and lateral compression, respectively. Dashed lines are guides to the eyes through the experimental data.

locked orientations, a situation in which most grains do not rotate any further.

At pressures of ~10 GPa, when $c/a \approx \sqrt{3}$, plastic deformation appears accommodated by a dominant basal slip and secondary pyramidal slip, with very little activity of prismatic slip. Do note, however, that textures at such conditions remain with a maximum near 0001, an orientation unfavorable for the activity of prismatic slip either during axial compression or lateral compression.

Finally, a previous study used density functional theory calculations to evaluate the effect of pressure on twin boundary formation energy for $\{10\bar{1}1\}$, $\{10\bar{1}2\}$, and $\{10\bar{1}3\}$ twins in Zn [17], concluding that the formation energy for $\{10\bar{1}2\}$ increases faster with pressure, exceeding that of $\{10\bar{1}1\}$ and $\{10\bar{1}3\}$ at pressures where $c/a < \sqrt{3}$. The authors hence suggested that pressure could change the twinning modes of Zn. As it stands, our data do not show evidence of activity on those additional twinning modes. The data at both low pressure, where $c/a > \sqrt{3}$, and higher pressure, where $c/a < \sqrt{3}$, is modeled well with a combination of slip and $\{10\bar{1}2\}$ twinning, with no need for an additional deformation mode. At ~10 GPa, when $c/a \approx \sqrt{3}$, $\{10\bar{1}2\}$ twins are not active during deformation and our measured textures do not reveal the substantial crystal reorientation with deformation which would be induced by twinning, and hence allow us to rule out the activation of supplementary twinning modes such as $\{10\bar{1}1\}$ or $\{10\bar{1}3\}$.

D. Strength of zinc under pressure

The strength of metals and their dependence on pressure, temperature, or strain rate is a fundamental property to model the materials' behavior under extreme conditions [34–37]. Figure 9 reports the ranges of differential stress modeled in EVPSC during sample axial and lateral compression (Figs. 5–7) as a function of pressure, i.e., the range within which the differential stress varies in the EVPSC calculations. The maximum strength that we deduce decreases from 4.7 to 3.6 GPa between 4.0 and 10.6 GPa hydrostatic pressure, and later increases to 9.3 GPa at 15.1 GPa. The strength of Zn hence seems to remain constant below hydrostatic pressures of ~10 GPa and the value of $c/a \approx \sqrt{3}$ and sharply increase when $c/a < \sqrt{3}$.

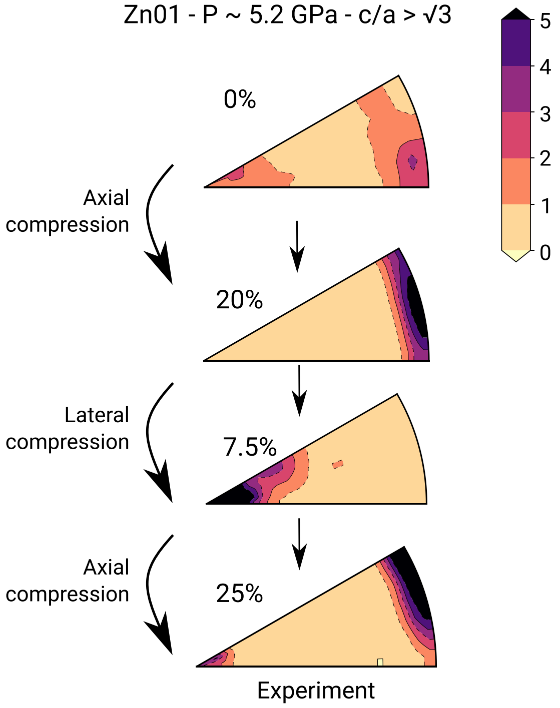

FIG. 10. Experimental texture for run Zn01. As in run D1653, performed at similar pressures, Zn develops a strong texture with prismatic planes perpendicular to compression upon compression. Upon lateral compression (sample lengthening), the texture rotates with the c axis becoming perpendicular to the compression direction. Subtle differences between runs Zn01 and D1653 are due to the different starting textures in both runs and the smaller beam size in run Zn01 leading to a lesser statically relevant number of grains within the beam.

In most cases, the strength of materials tends to scale with elasticity. One would hence expect a smooth increase of the measured maximum stress with pressure. At the microscopic scale, however, strength is controlled by the activation barrier and mobility of dislocations, and by the strength dislocation-dislocation and dislocation-boundaries interaction. It also depends on the sample texture. In particular, the maximum strength is reached once texture is fully developed, with most grains in orientation where stresses cannot be relaxed through mechanisms, such as twinning.

As such, our interpretation of the lower apparent strength of Zn at ≈10 GPa may be related to the absence of twinning activity in this pressure range. Twinning induces a large crystal reorientation with deformation with a near 90° rotation of the crystal c axes. These fast rotations, however, generate locked orientations, a situation in which most grains do not rotate any further. This does not happen in the ≈10 GPa pressure range, in which deformation is dominated by basal slip and secondary pyramidal slip, which only induce small crystal rotations.

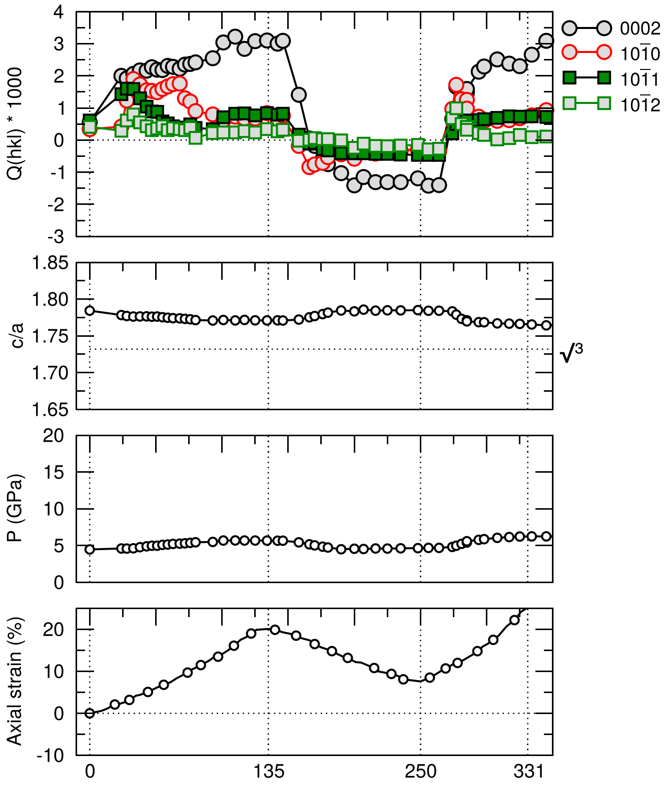

FIG. 11. Experimental results for run Zn01. (a) Experimental Q factors, (b) Zn c/a ratio, (c) pressure, and (d) total applied strain vs time.

V. CONCLUSION

In this work, we used hydrostatic pressure to vary the c/a ratio of Zn and study the effect on $\{10\bar{1}2\}$ deformation twins. In fact, our study demonstrates that pressure highlights the androgynous nature of $\{10\bar{1}2\}$ twins in Zn, which are compressive at low pressure, when $c/a > \sqrt{3}$, and tensile above 10 GPa, when $c/a < \sqrt{3}$. Beside $\{10\bar{1}2\}$ twins, the plasticity of Zn is controlled by a combination of basal, prismatic, and pyramidal $\langle c + a \rangle$ slip, depending on pressure and loading conditions.

At ~10 GPa, when $c/a \sim \sqrt{3}$, the activity of $\{10\bar{1}2\}$ twins is fully suppressed and the plasticity of Zn is fully controlled by basal and pyramidal $\langle c + a \rangle$ slip. As a consequence, there is no drastic reorientation of the crystal's c axes with deformation, and so there is little texture evolution in the cycles of axial and lateral compression, and a somewhat weaker material due to the lack of locked orientations induced by twinning. The activity of other $\{10\bar{1}n\}$ twinning modes, such as $\{10\bar{1}1\}$ or $\{10\bar{1}3\}$, which have been suggested to be present in Zn at high pressure is not observed.

This study also shows how hydrostatic pressure can be used to explore the dynamics of hcp metals beyond ambient conditions, conditions which challenge our conventional wisdom on the behavior of hcp metals. In this regard, the recent developments that allow for the investigation of twinning at the nanosecond timescale, and hence during shock compression [8,36,38], will offer new experimental opportunities to explore the fundamentals of metal plasticity, metals behavior in nonconventional applications, and the cores of planets and exoplanets.

All raw diffraction and sample images collected during the deformation experiments, along with the corresponding calibrations, have been deposited on the recherche.data.gouv.fr repository (see Ref. [39]). The archive also includes all input files for the EVPSC calculations along with spreadsheet tabulated results of all figures in the paper.

ACKNOWLEDGMENTS

The authors acknowledge the provision of beam time by the ESRF and APS and the support of W. Crichton during the ESRF experiments. They are thankful to Dr. Mingyu Gong for providing the dichromatic pattern figures and to A. Valovics and M. Thierry who performed a first version of the data processing while interns at Université Lille. This work was initiated under the U.S. Department of Energy, Office of Basic Energy Sciences Project No. FWP 06SCPE401, which funded C.N.T. In addition, S.M. and N.H. are funded by the European Union (ERC, HotCores, Grant No. 101054994). Views and opinions expressed are, however, those of the author(s) only and do not necessarily reflect those of the European Union or the European Research Council. Neither the European Union nor the granting authority can be held responsible for them. Portions of this work were performed at GeoSoilEnviroCARS (The University of Chicago, Sector 13), Advanced Photon Source, Argonne National Laboratory. GeoSoilEnviroCARS is supported by the National Science Foundation–Earth Sciences via SEES: Synchrotron Earth and Environmental Science (EAR Grant No. 2223273). This research used resources of the Advanced Photon Source, a U.S. Department of Energy (DOE) Office of Science User Facility operated for the DOE Office of Science by Argonne National Laboratory under Contract No. DE-AC02-06CH11357.

APPENDIX: ADDITIONAL FIGURES

Please refer to Figs. 10 and 11 for experimental texture and results for run Zn01.

---

[1] C. Cui, B. Hu, L. Zhao, and S. Liu, Titanium alloy production technology, market prospects and industry development, Mater. Des. **32**, 1684 (2011).

[2] A. A. Luo, Magnesium casting technology for structural applications, J. Magnes. Alloys **1**, 2 (2013).

[3] T. B. Britton, F. P. E. Dunne, and A. J. Wilkinson, On the mechanistic basis of deformation at the microscale in hexagonal close-packed metals, Proc. R. Soc. A. **471**, 20140881 (2015).

[4] R. G. Kraus, R. J. Hemley, S. J. Ali, J. L. Belof, L. X. Benedict, J. Bernier, D. Braun, R. E. Cohen, G. W. Collins, F. Coppari, M. P. Desjarlais, D. Fratanduono, S. Hamel, A. Krygier, A. Lazicki, J. Mcnaney, M. Millot, P. C. Myint, M. G. Newman, J. R. Rygg *et al.*, Measuring the melting curve of iron at super-earth core conditions, Science **375**, 202 (2022).

[5] M. H. Yoo, Slip, twinning, and fracture in hexagonal close-packed metals, Metall. Mater. Trans. A **12**, 409 (1981).

[6] H. Fan, S. Aubry, A. Arsenlis, and J. A. El-Awady, The role of twinning deformation on the hardening response of polycrystalline magnesium from discrete dislocation dynamics simulations, Acta Mater. **92**, 126 (2015).

[7] Q. Yu, Z.-W. Shan, J. Li, X. Huang, L. X. J. Sun, and E. Ma, Strong crystal size effect on deformation twinning, Nature (London) **463**, 335 (2010).

[8] S. Chen, Y. X. Li, N. B. Zhang, J. W. Huang, H. M. Hou, S. J. Ye, T. Zhong, X. L. Zeng, D. Fan, L. Lu, L. Wang, T. Sun, K. Fezzaa, Y. Y. Zhang, M. X. Tang, and S. N. Luo, Capture deformation twinning in Mg during shock compression with ultrafast synchrotron x-ray diffraction, Phys. Rev. Lett. **123**, 255501 (2019).

[9] R. Namakian and G. Z. Voyiadjis, An atomic displacive model for $\{10\bar{1}2\}\langle\bar{1}011\rangle$ twinning in hexagonal close packed metals with the emphasis on the role of partial stacking faults in formation of $\{10\bar{1}2\}$ twins, Acta Mater. **150**, 381 (2018).

[10] H. Vo, P. Pinney, M. Schneider, M. A. Kumar, R. McCabe, C. Tomé, and L. Capolungo, Automated characterization and classification of 3D microstructures: An application to 3D deformation twin networks in titanium, Mater. Today Adv. **20**, 100425 (2023).

[11] T. Kenichi, Structural study of Zn and Cd to ultrahigh pressures, Phys. Rev. B **56**, 5170 (1997).

[12] T. Kenichi, Absence of the *c*/*a* anomaly in Zn under high pressure with a helium-pressure medium, Phys. Rev. B **60**, 6171 (1999).

[13] K. Takemura, H. Yamawaki, H. Fujihisa, and T. Kikegawa, High-pressure x-ray studies of Zn at room and low temperatures with a He-pressure medium, High Press. Res. **22**, 337 (2002).

[14] D. Errandonea, S. G. MacLeod, J. Ruiz-Fuertes, L. Burakovsky, M. I. McMahon, C. W. Wilson, J. Ibañez, D. Daisenberger, and C. Popescu, High-pressure/high-temperature phase diagram of zinc, J. Phys.: Condens. Matter **30**, 295402 (2018).

[15] K. Takemura, The zinc story under high pressure, J. Miner. Mater. Charact. Eng. **07**, 354 (2019).

[16] W. Kanitpanyacharoen, S. Merkel, L. Miyagi, P. Kaercher, C. N. Tomé, Y. Wang, and H.-R. Wenk, Significance of mechanical twinning in hexagonal metals at high pressure, Acta Mater. **60**, 430 (2012).

[17] G. Liu, J. Wang, and Y. Shen, Density functional theory study of $\{10\bar{1}n\}$ twin boundaries of Zn under high pressure, Comput. Mater. Sci. **151**, 106 (2018).

[18] Y. Wang, W. B. Duhram, I. C. Getting, and D. J. Weidner, The deformation-DIA: A new apparatus for high temperature triaxial deformation to pressures up to 15 GPa, Rev. Sci. Instrum. **74**, 3002 (2003).

[19] J. Guignard and W. A. Crichton, The large volume press facility at ID06 beam line of the European Synchrotron Radiation Facility as a high pressure-high temperature deformation apparatus, Rev. Sci. Instrum. **86**, 085112 (2015).

[20] L. Lutterotti, R. Vasin, and H.-R. Wenk, Rietveld texture analysis from synchrotron diffraction images. I. Calibration and basic analysis, Powder Diffr. **29**, 76 (2014).

[21] H.-R. Wenk, L. Lutterotti, P. Kaercher, W. Kanitpanyacharoen, L. Miyagi, and R. Vasin, Rietveld texture analysis from synchrotron diffraction images. II. Complex multiphase materials and diamond anvil cell experiments, Powder Diffr. **29**, 220 (2014).

[22] A. K. Singh, The lattice strains in a specimen (cubic system) compressed nonhydrostatically in an opposed anvil device, J. Appl. Phys. **73**, 4278 (1993).

[23] A. K. Singh, C. Balasingh, H. K. Mao, R. J. Hemley, and J. Shu, Analysis of lattice strains measured under nonhydrostatic pressure, J. Appl. Phys. **83**, 7567 (1998).

[24] S. Merkel, N. Miyajima, D. Antonangeli, G. Fiquet, and T. Yagi, Lattice preferred orientation and stress in polycrystalline hcp-Co plastically deformed under high pressure, J. Appl. Phys. **100**, 023510 (2006).

[25] S. Merkel, C. N. Tomé, and H.-R. Wenk, A modeling analysis of the influence of plasticity on high pressure deformation of hcp-Co, Phys. Rev. B **79**, 064110 (2009).

[26] S. Merkel, M. Gruson, Y. Wang, N. Nishiyama, and C. N. Tomé, Texture and elastic strains in hcp-iron plastically deformed up to 17.5 GPa and 600 K: Experiment and model, Model. Simul. Mater. Sci. Eng. **20**, 024005 (2012).

[27] F. Lin, N. Hilairet, P. Raterron, A. Addad, J. Immoor, H. Marquardt, C. Tomé, L. Miyagi, and S. Merkel, Elasto-viscoplastic self consistent modeling of the ambient temperature plastic behavior of periclase deformed up to 5.4 GPa, J. Appl. Phys. **122**, 205902 (2017).

[28] S. R. Agnew, D. W. Brown, and C. N. Tomé, Validating a polycrystal model for the elastoplastic response of magnesium alloy AZ31 using *in situ* neutron diffraction, Acta Mater. **54**, 4841 (2006).

[29] B. Clausen, C. N. Tomé, D. W. Brown, and S. R. Agnew, Reorientation and stress relaxation due to twinning: Modeling and experimental characterization for Mg, Acta Mater. **56**, 2456 (2008).

[30] H. Wang, P. D. Wu, C. N. Tomé, and Y. Huang, A finite strain elastic-viscoplastic self-consistent model for polycrystalline materials, J. Mech. Phys. Solids **58**, 594 (2010).

[31] C. N. Tomé, R. A. Lebensohn, and U. F. Kocks, A model for texture development dominated by deformation twinning: Application to zirconium alloy, Acta Metal. Mater. **39**, 2667 (1991).

[32] A. Molinari, S. Ahzi, and R. Kouddane, On the self-consistent modeling of elastic-plastic behavior of polycrystals, Mech. Mater. **26**, 43 (1997).

[33] C. N. Tomé and R. A. Lebensohn, *Material Modeling with the Visco-plastic Self-consistent (VPSC) Approach* (Elsevier, Amsterdam, 2023), Chap. 4.2.5.

[34] R. Jeanloz, B. K. Godwal, and C. Meade, Static strength and equation of state of rhenium at ultra-high pressures, Nature (London) **349**, 687 (1991).

[35] M. B. Weinberger, S. H. Tolbert, and A. Kavner, Osmium metal studied under high pressure and nonhydrostatic stress, Phys. Rev. Lett. **100**, 045506 (2008).

[36] S. Merkel, S. Hok, C. Bolme, D. Rittman, K. J. Ramos, B. Morrow, H. J. Lee, B. Nagler, E. Galtier, E. Granados, A. Hashim, W. L. Mao, and A. E. Gleason, Femtosecond visualization of hcp-iron strength and plasticity under shock compression, Phys. Rev. Lett. **127**, 205501 (2021).

[37] C. Perreault, L. Q. Huston, K. Burrage, S. C. Couper, L. Miyagi, E. K. Moss, J. S. Pigott, J. S. Smith, N. Velisavljevic, Y. Vohra, and B. T. Sturtevant, Strength of tantalum to 276GPa determined by two x-ray diffraction techniques using diamond anvil cells, J. Appl. Phys. **131**, 015905 (2022).

[38] C. E. Wehrenberg, D. McGonegle, C. Bolme, A. Higginbotham, A. Lazicki, H. J. Lee, B. Nagler, H.-S. Park, B. A. Remington, R. E. Rudd, M. Sliwa, M. Suggit, D. Swift, F. Tavella, L. Zepeda-Ruiz, and J. S. Wark, *In situ* x-ray diffraction measurement of shock-wave-driven twinning and lattice dynamics, Nature (London) **550**, 496 (2017).

[39] S. Merkel, N. Hilairet, Y. Wang, J. Guignard, and C. Tomé, The androgynous twins of zinc - raw data and models, Recherche Data Gouv (2024), https://doi.org/10.57745/FOINIM.